RESEARCH ARTICLE

Editor's Choice

ADVANCED FUNCTIONAL MATERIALS

www.afm-journal.de

Self-Stratifying Colorful Low-Emissivity Paint for Thermal Regulation and Energy Saving

*Yilin Wang, Guowei Tang, Xuexue Xiang, Mulin Qin, Yu Qiu, Jian-Cheng Lai, and Yucan Peng**

Low-emissivity materials are regarded as promising candidates for thermal insulation. However, aesthetic concerns often hinder their practical application, primarily due to metallic gray coloration. While some colorful low-emissivity paints have been developed to address this issue, the labor application costs and complex preparation processes remain significant drawbacks. Here, a new category of self-stratifying colorful low-emissivity paints (SSCLPs) is presented, engineered to spontaneously form a distinct bilayer structure with a single application, thus eliminating the need for a second coat. Through careful formulation, the resulting bilayer coating features a highly reflective bottom layer and an infrared (IR)-transparent colored top layer, demonstrating low mid-infrared emissivity (as low as 0.107), high near-infrared reflectance (up to 0.814), and selectively visible reflectance for desired colors. Simulations confirm that effective stratification is essential for achieving the desired optical properties. Thermal insulation experiments demonstrate that SSCLPs can efficiently resist radiative heat transfer. Furthermore, building energy simulations indicate that SSCLP application to a two-story office building can yield annual heating, ventilation and air conditioning (HVAC) savings of up to 13.38 MJ m^{-2}, with an associated CO_2 emission reduction of 1.1 kg m^{-2}. This study contributes to advancing thermal insulation materials that promote energy savings and sustainability objectives.

1. Introduction

Energy shortages and excessive CO_2 emissions are pressing global concerns, highlighting the urgent need to reduce energy consumption. A substantial share of energy is devoted to heating and cooling to maintain appropriate temperatures in various environments, including buildings, transportation, storage, breeding, and brewing industries.[1–7] Among various thermal regulation strategies, heat insulation materials play a crucial role in enhancing energy efficiency by reducing heat transfer.[8] For instance, in buildings, heat insulation materials can significantly reduce energy consumption for heating and cooling by effectively limiting heat loss in winter and preventing excessive heat gain in summer.[9] This thermal barrier effect not only stabilizes indoor temperatures but also reduces dependency on active heating and cooling systems, ultimately contributing to energy conservation and a reduction in greenhouse gas emissions across diverse climates and applications.[10]

Low-thermal-conductivity materials are commonly used for heat insulation, owing to their ability to inhibit thermal conduction. To realize satisfied insulation, these materials are often designed with high porosity to trap pockets of still air, which enhances thermal resistance.[11–18] Based on their working mechanism, a few millimeters to centimeters of material thickness is typically required for adequate insulation.[8] In contrast, low-emissivity materials provide insulation by altering surface radiative properties.[19,20] Their low emissivity, i.e., high reflectance, can massively reduce thermal radiation exchange, thus enhancing heat insulation through radiation control.[21]

Low-emissivity coatings are usually classified into transparent and opaque types based on their applications.[22–24]

Y. Wang, G. Tang, X. Xiang, Y. Peng
Department of Energy and Resources Engineering
College of Engineering
Peking University
Beijing 100871, P. R. China
E-mail: yucan.peng@pku.edu.cn

X. Xiang
College of Textiles
Donghua University
Shanghai 201620, P. R. China

The ORCID identification number(s) for the author(s) of this article can be found under https://doi.org/10.1002/adfm.202507409

DOI: 10.1002/adfm.202507409

M. Qin
School of Materials Science and Engineering
Peking University
Beijing 100871, P. R. China

Y. Qiu
School of Energy Science and Engineering
Central South University
Changsha, Hunan 410083, P. R. China

J.-C. Lai
Tachin Technology Co., Ltd
Beijing 100094, P. R. China

J.-C. Lai
Beijing Institute of Collaborative Innovation
Beijing 100094, P. R. China

Transparent low-emissivity coatings are commonly used on windows to allow visible (VIS) light transmission while reflecting infrared radiation, enhancing energy efficiency without altering the appearance.[25] On the other hand, opaque ones often exhibit a metallic silver or gray appearance, which leads to aesthetic limitations and potential light pollution.[26,27] In many practical applications, visual appeal is as important as thermal performance, creating an urgent need for colorful low-emissivity coatings that combine effective insulation with aesthetic effect.[28]

To tackle this challenge, researchers have explored some approaches for colorful low-emissivity materials, such as surface modification, material mixing, and layer lamination. For example, Yuan et al. designed core-shell aluminum (Al) /Fe_3O_4 black composite pigments with an infrared emissivity of 0.50 in the 8–14 µm range.[29] Tan et al. prepared greenish-yellow coatings using Prussian blue (PB) surface-modified Al powders, achieving an average emissivity of 0.426 in the same spectral range.[30] Besides, Fantucci et al. mixed commercial Al paint with matte paints, resulting in ≈0.60 emissivity.[31] However, the emissivity levels are not sufficiently low to gratify effective heat insulation performance, and the resulting colors often fall short of aesthetic expectations. Recently, Peng et al. reported a colorful low-emissivity paint with ≈0.2 mid-infrared (MIR) emissivity.[32] Nevertheless, this approach requires two separate spray processes to form a bilayer laminated structure, increasing labor costs and application complexity.

Here, we propose self-stratifying colorful low-emissivity paints (SSCLPs) that spontaneously separate into a distinct bilayer structure, offering low emissivity and colorful appearance. However, the state-of-the-art self-stratifying coatings typically feature high emissivity.[33,34] More detailed performance comparisons between them are presented in Table S1 (Supporting Information). As shown in **Figure 1a**, the exemplary optical properties of colorful low-emissivity paints (CLPs) include high reflectance in both near-infrared (NIR) and MIR wavelength ranges, along with selective reflectance in the VIS spectrum. The desired color is achieved through this selective reflectance in the VIS range. In hot conditions, the high NIR and MIR reflectance of CLPs can effectively prevent solar heat and outdoor warmth from entering indoor spaces, thereby reducing heat gain and cooling energy consumption. Conversely, in cold conditions, the high MIR reflectance helps retain indoor heat, minimizing heat loss and energy consumption for heating.

2. Results and Discussion

2.1. Material Design and Self-Stratifying Principle

To achieve the desired optical spectrum, it is essential to select appropriate functional materials for the top and bottom layers in the self-stratified coating. For the bottom layer, we chose aluminum microflakes (Al MFs) as the reflective components, which can present high broadband reflectance as long as their directional arrangement is realized. Small-size flake Al pigment leads to high surface roughness, which will result in low specular reflectance and high-diffusing reflectance, leading to low total MIR reflectance.[35] After optimization, Al MFs with a size of 60 µm were selected (Note S1 and Figure S1, Supporting Information). To obtain the colorful appearance without compromising the IR reflectance of the bottom layer, nanoscale inorganic pigments were selected, including PB for blue, iron oxide (Fe_2O_3) for red, and goethite (α-FeOOH) for yellow.

To facilitate self-stratification, solvents with different properties were chosen for the top and bottom layer coatings. Due to the hydrophobicity of the Al MFs (Figure S2, Supporting Information), a non-polar perchloroethylene (PCE) solvent was employed to disperse Al MFs. Notably, the choice of solvent is critical in guiding the assembly morphology of Al MFs as well, which consequently affects the apparent reflectance of the resulting coating. On the contrary, pigment nanoparticles disperse more easily in polar solvents due to the formation of hydrogen bonds. Therefore, a mixed solvent of isopropyl alcohol (IPA) and water (volume ratio = 1:1) was selected for the top layer. Additionally, solvent density was carefully considered. As a result, the different polarities and densities of the solvents facilitate spontaneous separation, bringing the functional materials into distinct two layers. Overall, the rationale behind the optimization of the paint formula was to achieve a composition that enables self-stratification, presents a decent color appearance, and provides high IR reflectance simultaneously. For instance, the optimized ratio of Al MFs mass (g): PCE volume (mL) = 11:55. (See Note S1, Figures S3 and S4 for more detailed data on formula optimization, Supporting Information). With an increased usage of pigment nanoparticles, the coatings exhibit darker color shades alongside reduced MIR and NIR reflectivity. Additional information is provided in Note S1 and Figure S5–S13 (Supporting Information). In the main text, we present SSCLP samples with medium color shades as representatives.

Moreover, compatible polymer binders were chosen and incorporated into the SSCLPs to provide adhesion. Polyvinyl butyral (PVB) was utilized in the bottom oily layer due to its solubility in less polar solvents. To prevent the dissolution of PVB in the upper polar solvent, 1,1,2,2-tetrachloroethane (TCE) solvent was introduced to ensure the complete dissolution of PVB in the oily layer. The optimization of the PVB/TCE ratio is detailed in Note S1 and illustrated in Figures S14 and S15 (Supporting Information). For the aqueous layer, polyvinyl alcohol (PVA) was selected as the binder, as its numerous hydroxyl (-OH) groups can form hydrogen bonds with polar solvents, enhancing cohesiveness (See Note S1 and Figure S16 for more details, Supporting Information).

In SSCLPs, the functional components, binder polymers, and solvents are mixed homogenously upon using (Figure 1b). This process mirrors the shaking procedure typically used in the practical application of paints. The subsequent self-stratification process is depicted in Figure 1c. Due to their higher densities, PCE and TCE descend, bringing Al MFs and PVB into the bottom layer. In contrast, water and IPA containing inorganic pigment nanoparticles and PVA move upward to form the top layer. Ultimately, this results in two distinct layers: the top layer contains IPA, water, pigment nanoparticles, and PVA, while the bottom layer comprises PCE, TCE, Al MFs, and PVB, as shown in Figure 1d. Upon solvent evaporation, the bilayer coating is formed, exhibiting selective reflectance in the visible range and high reflectance in both NIR and MIR wavelength ranges, as illustrated in Figure 1e.

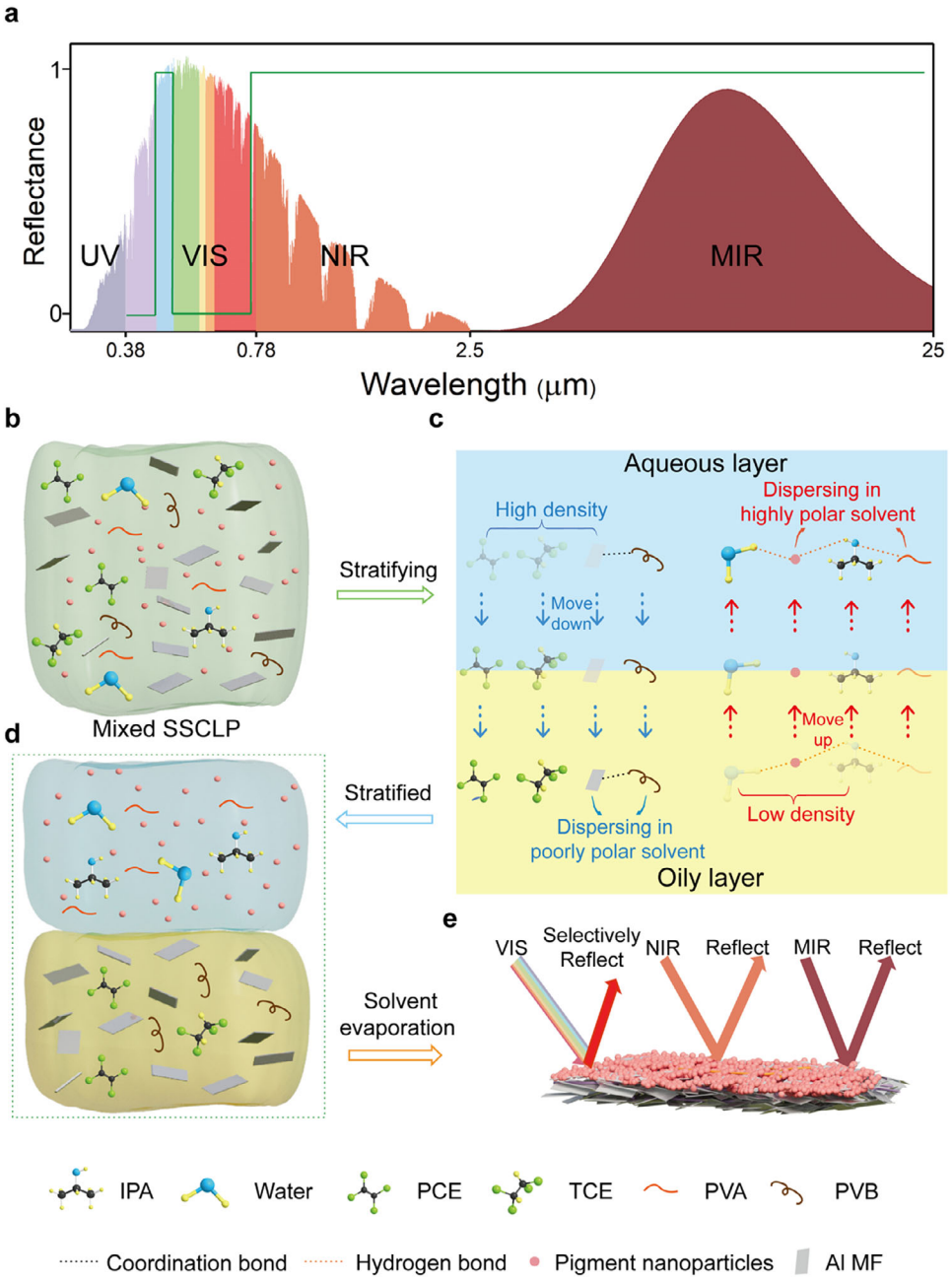

Figure 1. Design principles of self-stratifying colorful low-emissivity paints (SSCLPs). a) An exemplary reflectance spectrum of colorful low-emissivity paints. The green lines represent the spectrum of an ideal colorful low-emissivity paint. b) Schematic of a uniformly mixed SSCLP. c) Graphical explanation of the self-stratifying principle of SSCLP. The differences in polarity and density of solvents and fillers result in the self-stratification of paints. d) The stratified SSCLP. The top layer solution is low-density and high-polarity solvents that dissolve PVA binder and disperse pigment nanoparticles. The bottom layer solution is high-density and poor-polarity solvents that dissolve PVB binder and disperse Al MFs. e) Schematic of the bilayer coating formed by SSCLP.

2.2. Optical Performance of SSCLPs

Figure 2a displays the photographs of SSCLPs in both mixed and stratified conditions, revealing a range of colors, including red, blue, and yellow, offering viable alternatives to commercial paints. Here, sprayed-coated samples on glass substrates are presented as well. We refer to the SSCLPs by their respective colors, such as "red-SSCLP". Other colors can be obtained by mixing the three existing inorganic pigment nanoparticles. For example, we obtained a green color by mixing α-FeOOH and PB in a 1:1 mass ratio, an indigo color by mixing Fe_2O_3 and PB in a 2:1 mass ratio, and an orange color by mixing Fe_2O_3 and α-FeOOH in a 2:1 mass ratio. The photographs of the samples are demonstrated in Figure S17 (Supporting Information), and the

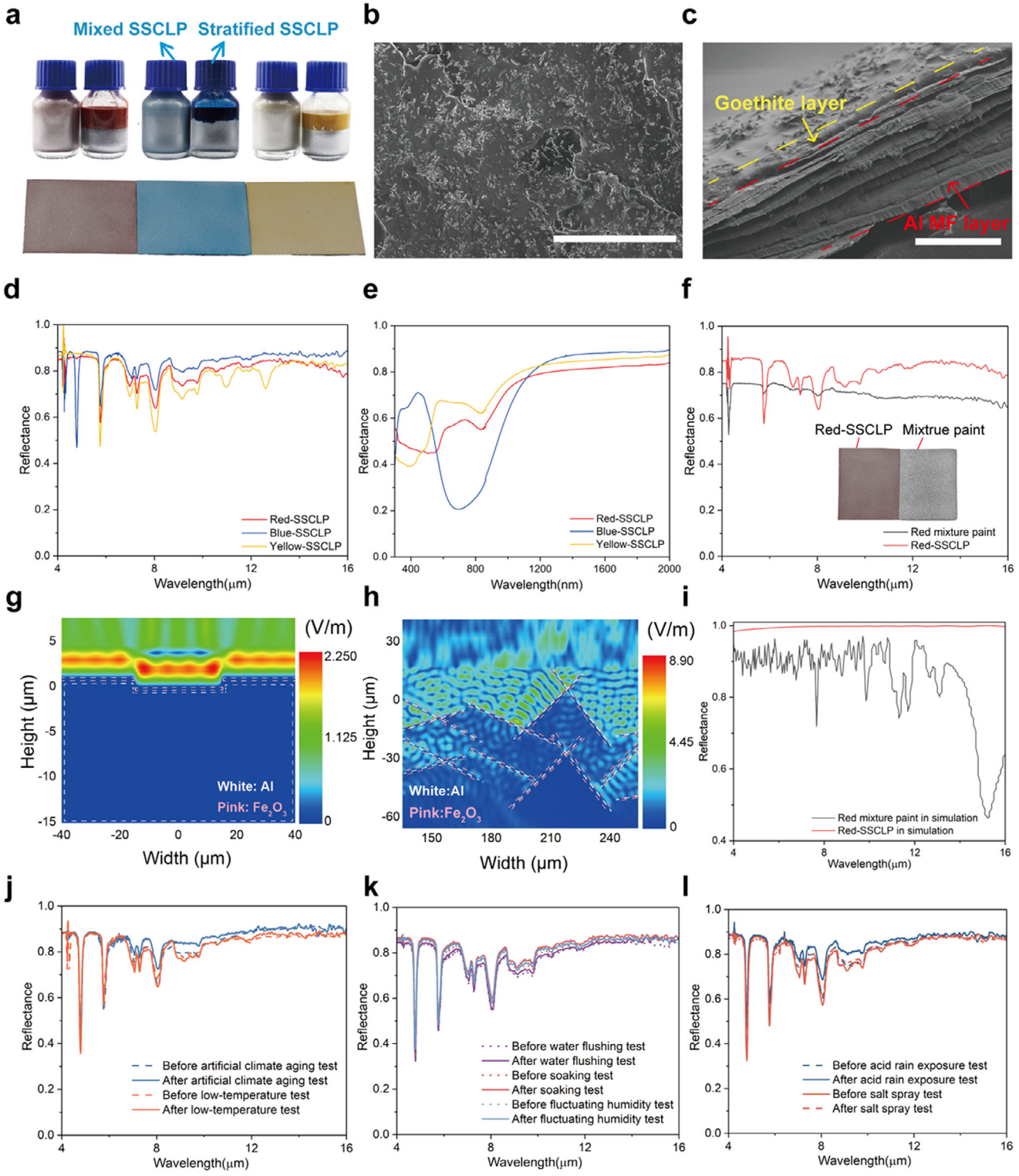

corresponding total MIR reflectance is demonstrated in Figure S18 (Supporting Information). Figure 2b presents a scanning electron microscope (SEM) image showcasing the surface morphology of the yellow-SSCLP, demonstrating the uniform distribution of goethite nanorods on the densely packed Al MFs. As shown in Figure 2c, the thickness of the Al MF layer and the goethite layer is ≈13 and 2 μm, respectively. This cross-section SEM image further verifies the successful self-stratification of the SSCLP.

As exhibited in Figure 2d, the total MIR reflectance for the SSCLP coating in three colors reach 0.893 for blue-SSCLP, 0.839 for red-SSCLP, and 0.862 for yellow-SSCLP, corresponding to emissivity of 0.107, 0.161 and 0.138 respectively, as measured by a Fourier transform infrared (FTIR) spectrometer equipped with a diffuse gold integrating sphere. The above calculated MIR reflectance is the weighted average value based on the blackbody radiation spectrum at the temperature of 300 K. The coating consisting solely of the Al MF layer shows ≈0.955 reflectance, as displayed in Figure S19 (Supporting Information). More details about the Al MF orientation distribution and its contribution to reflectance properties are presented in Note S2 (Supporting Information), Figure S20–S23 and Table S2 (Supporting Information). The observed reduction in total MIR reflectance is attributed to the inevitable thermal absorption by the binder polymers, pigment nanoparticles, and porous morphology of the top layer coating. In contrast, the average total MIR reflectance of commercial paints of the same thickness is only ≈0.08, which is significantly lower than that of SSCLPs (Figure S24a, Supporting Information), as these commercial paints tend to strongly absorb thermal radiation. Regarding the VIS and NIR wavelength ranges, Figure 2e presents the measured total reflectance of SSCLPs using an Ultraviolet (UV)-VIS-NIR spectrometer equipped with a diffuse reflectance accessory. The spectra for red, blue, and yellow-SSCLPs indicate NIR reflectance of ≈0.771 for blue-SSCLP, 0.814 for yellow-SSCLP, and 0.773 for red-SSCLP, along with characteristic reflection peaks corresponding to their respective colors in the VIS range. In comparison, commercial paints of the same colors and thickness show NIR reflectance ranging from 0.281 to 0.351, which are lower than those of the SSCLPs (Figure S24b, Supporting Information).

In addition, we compared the spectra of a simple mixture of Al MFs and Fe_2O_3 with those of red-SSCLP, using the same amounts of Al MFs and Fe_2O_3. As shown in Figure 2f, the MIR reflectance of the mixture paint is obviously lower than that of red-SSCLP, which can be attributed to the chaotic arrangement and orientation of Al MFs, as evidenced by the SEM image of the mixture paint (Figure S25, Supporting Information). This finding suggests that the MIR reflectance of stratified layer structure is superior. The VIS and NIR reflectance characteristics of the mixture paint are detailed in Figure S26 of the Supporting Information. Furthermore, the color intensity of the mixture paint is less pronounced compared to that of the SSCLP, as shown in the inset of Figure 2f. Besides, when comparing the colorful low-emissivity coating sprayed with a low-emissivity base layer followed by a color layer, the visual appearance and total MIR reflectance remain quite similar (Figures S27 and S28, Supporting Information).

To further explore the underlying mechanisms behind the improved reflectivity, we employed finite-difference time-domain (FDTD) simulations to investigate the differences in optical properties between the mixture paint structure and our SSCLP structure. The dispersions of electromagnetic field intensity at the wavelength of 8 μm are depicted in Figure 2g,h, illustrating the flow of radiation wave inside the coating structure. As shown in Figure 2g, incident radiation can be almost completely reflected from the coating surface due to the well-layered structure of Al MFs in SSCLP. Even with the presence of the pigment nanoparticles layer on the Al MF layer, the coating maintains high reflectance over the entire spectrum. In contrast, as shown in Figure 2h, the randomly distributed Al MFs structure in the mixture paint causes incident radiation to be reflected in various orientations. The pigment layer on the Al MF surface absorbs radiation that is reflected from adjacent Al MFs, resulting in lower MIR reflectance for the mixture paint. Corresponding reflectance over 4–16 μm wavelengths of SSCLP and mixture paint are shown in Figure 2i. The MIR reflectance of our SSCLP is higher than that of the mixture paint. The simulated reflectance is higher and exhibits fewer characteristic peaks compared to the experimental results, which can be attributed to the omission of PVA, PVB, and the porous structure in the simulations.

In addition, we also explored the VIS-NIR properties of the two structures. For the NIR band, the dispersion of electromagnetic field intensity at the wavelength of 1 μm and reflectance are illustrated in Figures S29–S31 of the Supporting Information, demonstrating that the NIR reflectance of our SSCLP is also higher than that of the mixture paint. Regarding the VIS band, for SSCLP, the characteristic peak in the VIS-NIR spectrum arises from the selective reflectance of the Fe_2O_3 layer, corresponding to the same peak observed in the experimental spectrum (Figure S31, Supporting Information). The deviation in the numerical values of these characteristic peaks arises because the simulation assumes a relatively ideal Fe_2O_3 layer, whereas in the

Figure 2. Optical properties of SSCLP and environmental durability tests. a) Photograph of the formulated SSCLP solutions in evenly mixed condition (left) and stratified condition (right), and coating samples on glass substrates. From left to right, red, blue, and yellow, respectively. b) SEM image of the bilayer coating formed by yellow-SSCLP, of which the bottom is the Al MF layer, and the top is the goethite nanorods layer. Scale bar, 50 μm. c) Cross-section SEM image of the bilayer coating formed by yellow-SSCLP. The red dashed lines locate the Al MF layer, and the yellow dashed lines locate the goethite layer. Scale bar, 10 μm. d) Measured total reflectance of SSCLP coating samples on glass substrates in the MIR wavelength range. e) Measured total reflectance of SSCLP coating samples on glass substrates in the visible and NIR wavelength range. f) Measured MIR reflectance for the red mixture paint and red-SSCLP. g) Map of electromagnetic field intensity for stratified red paint (red-SSCLP) at the wavelength of 8 μm. h) Map of electromagnetic field intensity for red mixture paint at the wavelength of 8 μm. i) Simulated total reflectance in the MIR wavelength range of red-SSCLP and red mixture paint. j) Measured MIR spectra for SSCLP coating samples before and after the artificial climate aging test (T = 47 °C, relative humidity = 96%, UV irradiation = 8.5 W m^{-2}) and low-temperature test (−20 °C). k) Measured MIR spectra for SSCLP coating samples before and after the water flushing test, soaking test, and fluctuating humidity test. l) Measured MIR spectra for samples before and after acid rain exposure test and salt spray test. No obvious spectral change was observed.

experiment, the pigment nanoparticles exhibited agglomeration rather than forming a continuous thin film, thereby weakening the characteristic peaks of the pigment material. For the mixture paint, the characteristic peak also aligns with the experimental results (Figure S31, Supporting Information). However, due to the random distribution of Al MFs in the mixture paint, the pigment material no longer forms a continuous film on the topmost incident layer. Therefore, the characteristic peaks of the pigment material are weakened in both the experimental and simulated results.

2.3. Durability Tests of SSCLPs

To assess the durability of SSCLPs, we conducted a series of tests involving the measurement of sample mass, MIR spectra, and visual inspections before and after specific environmental exposures. First, SSCLP coating samples were subjected to artificial climate aging ($T = 47$ °C, relative humidity = 96%, UV irradiation = 8.5 W m^{-2}) and low-temperature (−20 °C) environments for two weeks. As illustrated in Figure 2j, Figures S32 and S33 (Supporting Information), the SSCLPs exhibited remarkable stability, with no significant alterations observed in their MIR reflectance, mass, or visual appearance after the exposure period.

To assess adhesion, we tested SSCLP samples with varying PVA contents by placing them under an acrylic plate with a 1.1 kg object and then pulling the plate horizontally, as shown in Figure S34 (Supporting Information). We measured the weights of SSCLP samples before and after the test. The detailed mass information of samples before and after the adhesin test and mass loss ratios can be found in Table S3 (Supporting Information). The photographs of SSCLP samples before and after the adhesion test are shown in Figure S35 (Supporting Information). We selected 40 mg mL^{-1} as the optimized PVA concentration in IPA/water, balancing its satisfactory adhesion performance (≈2.6% mass loss with no visible appearance change) while minimizing the reduction in MIR reflectance.

In order to evaluate the durability of SSCLP against water, we performed the water flushing test, soaking test, and fluctuating humidity test. As shown in Figure 2k, Figures S32 and S33 (Supporting Information), there were no significant changes in MIR reflectance, mass, and appearance before and after the tests. Additionally, samples were tested in acid rain exposure and salt spray to evaluate their durability in corrosive environments. As shown in Figure 2l, Figures S32 and S33 (Supporting Information), the samples demonstrated decent durability with no significant changes in MIR reflectivity, mass, and appearance.

2.4. Heat Insulation Performance Demonstration

To visually demonstrate the thermal insulation performance of SSCLPs, we selected red-SSCLP as a representative sample and compared it with commercial red paint, both applied to glass substrates. As illustrated in **Figure 3a**, both samples were placed on a hot plate set to 40 °C, and their thermal profiles were captured using an infrared thermal camera. After reaching thermal equilibrium, both samples attained the same temperature of 40 °C. However, due to the difference in radiant heat emitted from their surfaces, the temperature displayed by the thermal camera differed. As shown in Figure 3b, the surface temperature recorded for the SSCLP is apparently lower, indicating that the SSCLP sample has a much lower IR emissivity.

Furthermore, we constructed cubic building simulants with the exterior surfaces of their walls and roofs coated with red-SSCLP and commercial red paint, respectively. As depicted in Figure 3c, these simulants were placed in a vacuum oven set at 50 °C. The temperature of the vacuum oven is defined as T_{amb}. Thermocouples were installed at designated positions within each building simulant to measure the internal temperature (denoted as T_{in}). To prevent thermal conduction from the oven floor, an insulating foam board was placed beneath the simulants. In the vacuum chamber, the absence of air minimizes heat transfer via convection, making thermal radiation the primary mode of heat transfer. As shown in Figure 3d, the simulant coated with red-SSCLP exhibited a significantly slower increase in internal air temperature compared to the one coated with commercial red paint. At 677 s, the measured T_{in} of red-SSCLP was 5.1 °C lower than that of commercial red paint, validating the effectiveness of SSCLP in reducing heat exchange through thermal radiation.

Additionally, we evaluated the thermal insulation performance of the building simulants coated with red-SSCLP and commercial red paint under standard room-temperature conditions (24 °C). As illustrated in Figure 3e, ice cream samples with almost identical initial mass before tests (≈18 g) were placed in glass containers inside each building simulant. After 1 h, we measured the mass loss of ice creams to assess the extent of melting, as shown in Figure 3f. With exterior and interior coatings, the ice creams within the red-SSCLP-coated simulant revealed a reduced mass loss rate of ≈38.5% compared to that within the commercial red paint-coated simulant. This substantial reduction indicates that the red-SSCLP effectively slowed down the melting rate due to its superior heat insulation properties. Figure 3g presents photographs of the ice cream samples before and after the 1 h testing period, further demonstrating the enhanced thermal insulation provided by SSCLPs.

2.5. Building Energy Saving Calculations

To quantitatively evaluate the potential energy-saving impact of SSCLPs, we developed a building model that incorporates the optical properties of the materials and real weather data from various regions in China, utilizing commercial building energy simulation software DEST. We analyzed multiple cities across different climate zones to calculate the annual energy savings for a two-story office building when SSCLPs are applied to exterior and interior walls and roofs. Detailed information about the calculations and the building model can be found in Methods, Figure S36, and Table S4 (Supporting Information). We calculated the annual heating, ventilation, and air conditioning (HVAC) consumption of the building model with and without our SSCLPs to obtain HVAC savings. In this model, both heating and cooling are provided by an air conditioner with a coefficient of performance (COP) of 3.

To investigate the impact of different colors of SSCLPs on energy savings in various climatic zones, we selected ten cities in different climatic zones (Hot summer & cold winter zones:

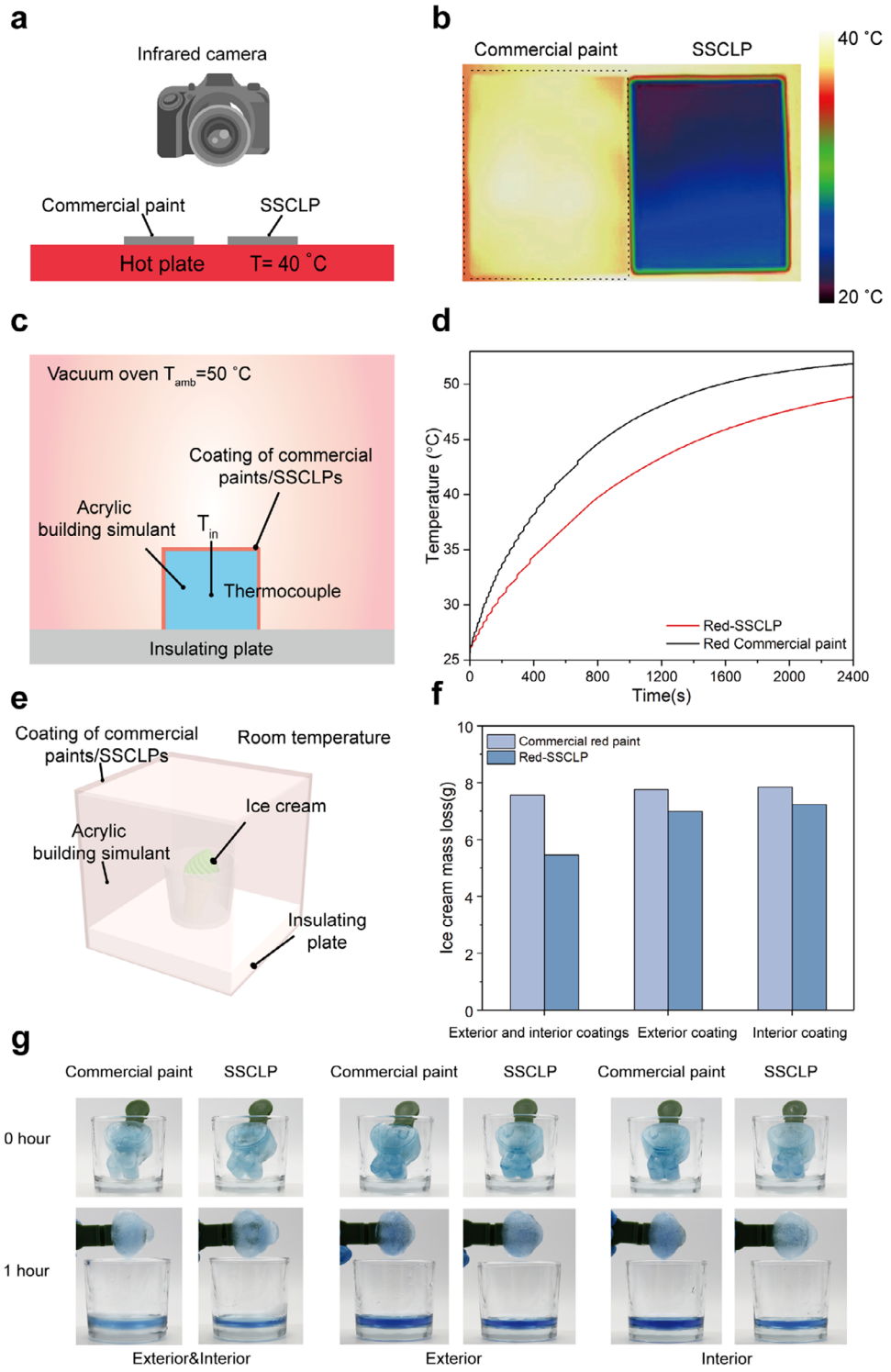

Figure 3. Heat insulation demonstration of SSCLP. a) Schematic of the experiment examining the surface temperatures of samples on a hot stage. b) Infrared thermal images of commercial red paint (left) and red-SSCLP (right) on the same hot stage. c) Schematic of building a simulant test in a 50 °C vacuum oven. Thermocouples were employed to measure the T_{in} of the building simulants. d) Measured internal temperature curves of the building simulants with exterior walls and roofs coated with different surface modifications. The simulant with the red-SSCLP exhibited a slower temperature increase. e) Schematic of ice cream tests within the building simulants. Ice cream samples were placed in a glass container inside the building, simulants were coated with different paints under standard room-temperature conditions. f) Measured mass loss of ice cream samples after 1 h for different surface modifications. g) Photographs of ice cream samples before and after 1 hour inside the building, simulants coated with different coatings. The initial weight of all ice creams is ≈18 g.

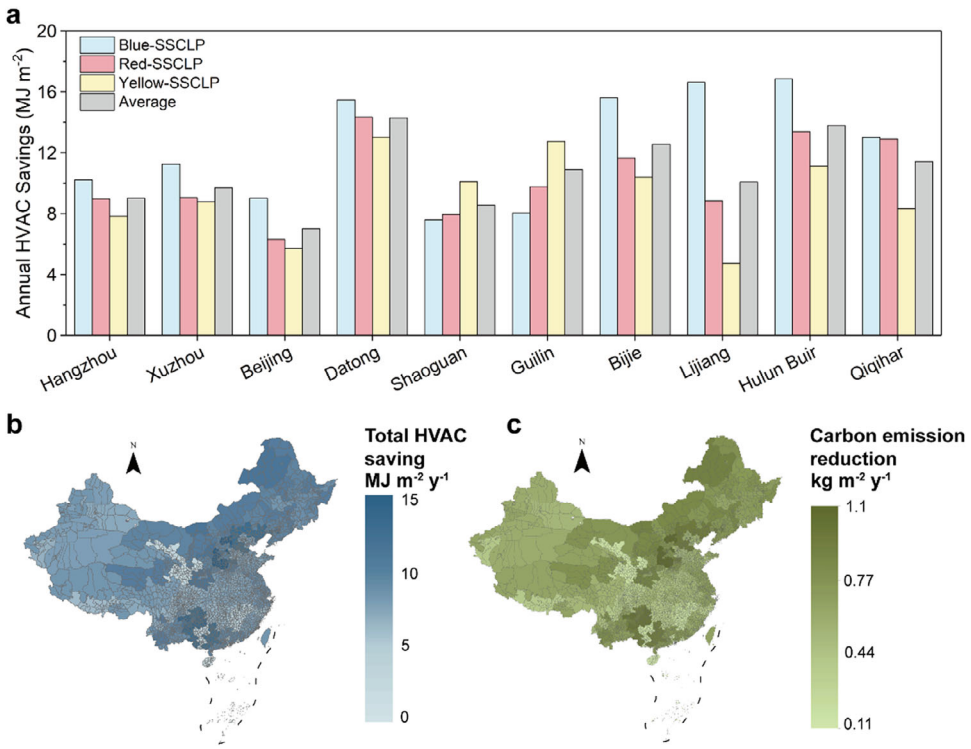

Figure 4. Evaluation of building energy savings by applying SSCLPs. a) Annual total energy saving for a two-story office building coated with various colors of SSCLPs and corresponding to the average of the three-color parameters in ten selected cities across various climate zones. b) Calculated color map of annual total HVAC savings for a two-story office building in different climates, with both exterior and interior walls and roofs coated with average SSCLP. c) Calculated color map of corresponding annual CO_2 emission reduction.

Hangzhou and Xuzhou, Cold zones: Beijing and Datong, Temperate zones: Bijie and Lijiang, Hot summer & warm winter zones: Shaoguan and Guilin, Severe cold zones: Hulun Buir and Qiqihar) and calculated the total annual HVAC savings of buildings coated with SSCLPs of different colors (blue: solar reflectance: 0.506, emissivity: 0.1066; red: solar reflectance: 0.591, emissivity: 0.1613; yellow: solar reflectance: 0.655, emissivity: 0.1379, and corresponding to the average of the three color-SSCLPs' parameters: solar reflectance: 0.584, emissivity: 0.135).

As shown in **Figure** 4a, the application of SSCLPs in different colors to building walls and roofs has shown significant year-round HVAC energy savings. Specifically, in most regions of China except the hot summer & warm winter region, the total HVAC energy savings decrease as the solar reflectance increases. This is because higher solar reflectance reduces the absorption of heat from sunlight, leading to increased heating energy consumption in winter, even though it reduces cooling energy consumption in summer. The ambient temperatures during winter that necessitate heating are quite low, leading to an increased demand for heating when solar heat gain is minimal. Moreover, although summer temperatures can be relatively high, solar irradiation is not intense due to predominantly cloudy and rainy weather. Consequently, the total HVAC energy savings are largely dependent on heating energy savings. Therefore, the impact of increased solar reflectance on reducing heating energy savings is greater than the improvement in cooling energy savings, even if the solar reflectance of these low-emissivity coatings is greater than 0.5. In contrast, in the hot summer & warm winter regions, the total HVAC energy savings increase with higher solar reflectance. Due to the higher winter temperatures in these regions, heating energy consumption is inherently lower, making cooling energy dominant in HVAC energy consumption. Thus, SSCLPs with higher solar reflectance are more suitable for hot summer & warm winter regions.

We calculated the HVAC energy savings by applying SSCLPs to buildings in 101 cities in China and constructed the energy-saving map. Figure 4b illustrates the annual total HVAC savings. The annual total HVAC energy savings vary between 1.33 MJ m^{-2} in Dongfang, Hannan, and 13.38 MJ m^{-2} in Datong, Shanxi. The separate heating and cooling energy-saving maps are displayed in Figure S37a,b (Supporting Information), respectively. Significant heating energy savings are observed across all simulated zones. The application of SSCLPs yields positive cooling energy savings in certain regions, such as Wuwei, Gansu (0.984 MJ m^{-2}), where their high NIR reflectance reduces the solar heat gain, partially offsetting the limited sky radiative cooling caused by low MIR emissivity. However, in some cities, negative cooling energy savings are observed, primarily due to the reduced sky radiative cooling resulting from the low MIR emissivity, which outweighs the benefit of decreased solar absorption, but annual energy savings still remain positive. Overall, in the context of China's climate zones, the application of SSCLPs can achieve year-round HVAC energy savings. This is particularly evident in cold and mild climate zones. However, in regions with consistently high temperatures throughout the year, where heating demands are minimal, caution should be exercised due to the

potential loss of sky radiative cooling caused by the low emissivity of SSCLPs.

Figure 4c presents color maps of the annual CO_2 emission reductions associated with applying SSCLPs to walls and roofs, with reductions of up to 1.1 kg m^{-2}. The corresponding annual electric energy saving map is shown in Figure S38 (Supporting Information), indicating savings of up to 3.72 kWh m^{-2}. More detailed data on the annual CO_2 emission reductions for the selected ten cities are available in Table S5 (Supporting Information).

3. Conclusion

In this study, we report a self-stratifying approach to develop user-friendly colorful low-emissivity paints (SSCLPs) designed for effective thermal insulation. These SSCLPs achieve MIR reflectance up to 0.893 and NIR reflectance as high as 0.814, while maintaining aesthetic appeal through selective reflectance in the visible spectrum. Our simulation-based analysis highlights the impact of the mixing degree of aluminum microflakes (Al MFs) and pigment nanoparticles on the overall optical properties of the formed coatings. It demonstrates that improved stratification leads to enhanced MIR reflectance compared to evenly mixed formulations. In the heat insulation demonstration experiments, the SSCLP coatings effectively resisted heat input from the hot environment, significantly delaying the temperature increase in the building simulant. Meanwhile, it was observed that SSCLPs reduced the melting rate of ice creams by ≈38.5%. Using a two-story office building compliant with energy efficiency standards for public buildings as a model, our building energy simulations reveal substantial annual heating and cooling savings: total energy savings of up to 13.38 MJ m^{-2}, and a reduction of CO_2 emissions of up to 1.1 kg m^{-2}.

The SSCLPs provide an innovative solution for year-round HVAC energy savings involving both heating and cooling with a single installation. The scalable, solution-based process allows for easy application on various surfaces, such as roofs and walls, via spray coating. We believe that these self-stratifying, colorful, low-emissivity paints offer a transformative approach to energy efficiency across various sectors, including buildings, transportation, storage, livestock breeding, and brewing industries, thereby advancing efforts toward global carbon neutrality.

4. Experimental Section

Materials Synthesis and Fabrication: The Al MFs were provided by Guangdong Wanxing International Trade Co., Ltd. The pigment nanoparticles, including Prussian blue (Macklin, 99%), iron oxide (Macklin, 99%), and goethite (Aladdin, 30 to 63% Fe) were used as purchased. The solvents, including PCE (Macklin, 98%), TCE (TgLabor, 98%), and IPA (TgLabor, AR) were used as purchased without further purification. Commercial paints were purchased from Qisehua Coatings Co., Ltd. PVB was dissolved and stored in TCE at a concentration of 10 mg mL^{-1} before use, and PVA was dissolved and stored in IPA and water (solvent volume = 1:1) at a concentration of 40 mg mL^{-1} before use. Coating dispersions of a low-emissivity layer were needed to be prepared and a color layer, and then mix the two dispersions to form a self-stratifying colorful low-emissivity painting. A typical formulation for a low-emissivity oil layer dispersion includes 0.11 g Al MFs, 0.55 mL PCE, 0.11 mL PVB solution, and a formulation for a pigmented aqueous layer includes 0.005 g PB, 0.5 mL PVA solution, 0.05 mL IPA, and 0.05 mL water. The two were fully oscillated and sonicated, then mixed to form an SSCLP. A 40 × 50 × 1 millimeter glass was chosen as the substrate, rinsed with deionized water, ethanol, and acetone in turn, and finally blown dry with nitrogen gas. The spraying coating method was used to apply the paint on the substrate. The pressure of the spray gun was set at 200 KPa, with the tip of the spray gun located at ≈0.1 m from the substrate in a typical spraying process. A typical formulation for the mixture paint includes 0.11 g Al MFs, 0.01 g Fe_2O_3, 0.66 mL IPA, and 0.5 mL PVA. The solution was shaken before use. The same substrate and spray coating method as SSCLPs were used to prepare mixture paint samples. All samples were dried after the spray coating process.

Preparation of Cross-Section Samples: To facilitate cutting, yellow-SSCLP was sprayed on top of the Thermoplastic polyurethane (TPU) substrate according to the aforementioned spraying method, and the TPU substrate was cleaned in the same way as the glass above. The sample was placed on a clean platform with its substrate side facing out. A sharp blade (Gillette) was used to quickly cut the sample in a vertical direction to obtain the cross-sectional sample.

Characterization: Surface morphology images of the coatings were obtained by field emission scanning electron microscopy (SEM, Hitachi SU8220). MIR reflectance was characterized using a Fourier transform IR spectrometer (FTIR, Nicolet iS50) equipped with a diffuse gold integrating sphere (PIKE Technologies). Visible and NIR reflectance was measured by an ultraviolet-visible-near-IR spectrophotometer (UV–VIS-NIR, Lambda 1050+). Diffraction patterns of samples were recorded using an X-ray diffractometer (XRD, SmartLab, Rigaku) with an operating voltage and current of 40 kV/150 mA, a rotating copper target, an X-ray wavelength of 1.54188 Å, and a scanning angle range of 10° – 80°. Sample masses were measured with an analytical balance (Sartorius, 0.0001 g readability).

Optical Simulation: Reflectivity and electromagnetic field simulations were conducted using FDTD solutions. For both the mixture paint and SSCLP models, the upper and lower boundaries were set to be perfect matching layers to simulate open areas and prevent wave reflections from interfering with the results within the computational domain. The left and right boundaries were set to be periodic boundaries to simulate infinite periodic structures so that the boundaries of the computational domain were "connected" to each other, thereby accurately reflecting the physical properties of the painting structure. For the mixture paint model, the Al MFs were assigned a width of 50 µm and a thickness of 200 nm, each conformally wrapped with a 100 nm thick Fe_2O_3 layer. Based on the SEM images, the Al MFs were set to be randomly distributed in a 75 µm-thick region in the model. The x and y coordinates of the center point of the Al MFs, along with the angle between the aluminum sheet and the *x*-axis, were treated as random variables to generate a randomly distributed Al MF layer. The incident radiation source was set to be 15 µm above the upper boundary of the Al MFs region. For the SSCLP model, SEM images revealed that the Al MFs were stacked flat on top of each other; thus, the Al MFs as an entire layer were set with a thickness of 15 µm, covered with a 200 nm thick Fe_2O_3 layer. Moreover, a ladder-like structure with an overlap thickness of 200 nm was constructed to more accurately reflect the actual stacking state of the Al MFs in SSCLP. The incident radiation source was set to be 2 µm above the upper boundary of the pigment region.

Environmental Durability Tests: 1) Artificial climate aging test: The testing method was modified from GB/T 1740–2007 and GB/T 1865–2009. A dried sample was placed in a programmable environmental chamber with precise temperature and humidity control. The temperature was maintained at 47 °C constantly, while the relative humidity was maintained at 96% constantly. Meanwhile, a UV lamp was installed at a height of 10 cm above the sample with a wavelength of 340 nm and an intensity of ≈8.5 W m^{-2}. 2) Low-temperature test: A dried sample was placed in the refrigerator at a temperature of −20 °C. 3) Acid rain exposure test: The testing method was modified from ASTM D7356. Artificial acid rain (PH = 5) was prepared by mixing diluted sulfuric acid and diluted nitric acid, which was added into a humidifier. A dried sample was placed at the vapor outlet, at a distance of ≈15 cm, with a vapor rate of 300 mL h^{-1}. 4) Salt spray test: The

testing method was modified from GB/T 1771–2007. A NaCl aqueous solution with a concentration of 5 wt.% was added to the humidifier. A dried sample was placed at the vapor outlet, at a distance of ≈15 cm, with a vapor rate of 300 mL h^{-1}. 5) Soaking test: A dried sample was submerged in 250 mL of water. The above tests 1) –5) all lasted for two weeks. 6) Water flushing test: The testing method was modified from ASTM D7377. A dried sample was fixed at an inclination of ≈45° at a distance of 5 cm from a water faucet. Water was released at a flow rate of ≈120 mL min^{-1}, striking the sample before draining into a sink. The test duration was 2 h. 7) Fluctuating humidity test: A dried sample was placed in a programmable environmental chamber with precise temperature and humidity control. The temperature was maintained at a constant 25 °C, while the relative humidity was varied. Specifically, the relative humidity was sequentially adjusted as follows: 40% for 1 h, increased to 60% for 1 h, then to 80% for 1 h, and finally to 100% for 1 h. Subsequently, it decreased back to 80% for 1 h, then to 60% for 1 h, and finally returned to 40% for the last hour. 8) Mechanical abrasion evaluation: An SSCLP sample (glass substrate) was adhered to a table, with an acrylic plate and a 1.1 kg weight placed on top. The acrylic plate was then dragged horizontally across the SSCLP surface.

Heat Insulation Performance Demonstration: 1) Thermal imaging: Thermal images were captured using a thermal camera (HM-TP42-3AQF/W, HIKMICRO). Two identical glass substrates (50 × 40 × 1 millimeter) coated with red-SSCLP and commercial red paint, respectively, were placed on a hot plate set to 40 °C. 2) Vacuum oven test: For the thermal demonstration in a vacuum oven, cubic building simulants were constructed from acrylic boards (10 cm side length and 3 mm thick). The internal temperature was measured using thermocouples (K type, KAIPUSEN) inserted into the simulants and connected to a data logger (640X, KAIPUSEN). 3) Ice cream melting test: The building simulants used for this test were the same as the vacuum oven test. Water with blue food-grade pigment was added to the ice cream mold, frozen in the refrigerator at −20 °C for 2 days, and then unmolded to prepare the ice creams used in this experiment. The initial weights of the ice creams were all ≈18 g.

Building Energy Saving Calculations by DEST: DEST 2.0 software was used to conduct a detailed energy consumption simulation analysis for building applications. The building model was a two-story office building with a height of 3.6 meters, a length of 40 meters, a width of 14.63 meters, and a total air-conditioned area of 1140 square meters. The building was oriented due north, with window-to-wall ratios of 0.11 for the south façade and 0.12 for the north facade. The heat transfer coefficient for the exterior walls, roofs, and exterior windows was set according to the characteristics of different climate zones and in compliance with the provisions of the Energy Saving Design Standard for Public Buildings (DB37 5155-2019). The indoor HVAC system employs a stand-alone unit, which was used for cooling in summer and heating in winter. Regarding ventilation energy consumption, the frequency of indoor air changes at 0.5 times per hour in summer was set with air conditioning on, 2 times per hour without air conditioning, and 0.5 times per hour in winter with or without air conditioning. The indoor temperature was set to be 26 °C constantly. Typical annual outdoor meteorological data were utilized from DEST 2.0, including hourly temperature, relative humidity, wind direction, wind speed, and solar radiation throughout the year. According to the downloaded building model, the surface solar reflectivity values of the exterior walls, interior walls, and roofs were set at 0.22, 0.08, and 0.3, respectively, and the MIR emissivity was set at 0.85. To evaluate the effect of SSCLP applications, these parameters were updated using experimentally measured data: the average solar reflectance (380–2000 nm) and MIR emissivity of the SSCLPs in red, blue, and yellow were 0.584 and 0.135 (equal to 0.865 of average MIR reflectance), respectively. The weighted average solar reflectance values of SSCLPs were calculated based on the solar radiation spectrum. The weighted average MIR reflectance values of SSCLPs were calculated based on the blackbody radiation spectrum at 300 K. The annual HVAC, heating, cooling, and electric energy savings in 101 cities across China were calculated. Based on these data, the results were extrapolated to the surrounding areas. The thermal resistance of the exterior wall and interior wall of office building models in different climates is shown in Table S6 (Supporting Information).

Supporting Information

Supporting Information is available from the Wiley Online Library or from the author.

Acknowledgements

This work was supported by the National Natural Science Foundation of China (Grant No. 22475007).

Conflict of Interest

The authors declare no conflict of interest.

Data Availability Statement

The data that support the findings of this study are available from the corresponding author upon reasonable request.

Keywords

colorful low-emissivity paints, energy saving, self-stratification, thermal insulation, thermal radiation barrier

Received: March 24, 2025
Revised: April 21, 2025
Published online: May 19, 2025

[1] L. Filina-Dawidowicz, S. Filin, *Energy Efficiency* **2019**, *12*, 1151.
[2] E. A. Goldstein, A. P. Raman, S. Fan, *Nat. Energy* **2017**, *2*, 17143.
[3] A. P. Raman, M. Abou Anoma, L. Zhu, E. Rephaeli, S. Fan, *Nature* **2014**, *515*, 540.
[4] S. Chakraborty, A. C. Newton, *Plant Pathology* **2011**, *60*, 2.
[5] S. G. Mun, *International Journal of Hospitality Management* **2020**, *85*, 102432.
[6] G. Zhang, O. Steuer, R. Li, Y. Cheng, R. Huebner, M. Helm, S. Zhou, Y. Liu, S. Prucnal, *Appl. Surf. Sci.* **2024**, *648*, 159046.
[7] S. Zhong, B. Lu, D.-C. Wang, B. Arianpour, S. Wang, H. Han, J. Yin, H. Bao, Y. Liu, Z. Wen, Y. Zhou, *Adv. Mater.* **2025**, *37*, 2415386.
[8] B. P. Jelle, *Energy Build.* **2011**, *43*, 2549.
[9] Y. Peng, L. Fan, W. Jin, Y. Ye, Z. Huang, S. Zhai, X. Luo, Y. Ma, J. Tang, J. Zhou, L. C. Greenburg, A. Majumdar, S. Fan, Y. Cui, *Nat. Sustain.* **2022**, *5*, 339.
[10] M. Ibrahim, L. Bianco, O. Ibrahim, E. Wurtz, *Journal of Building Engineering* **2018**, *18*, 454.
[11] E. Abraham, V. Cherpak, B. Senyuk, J. B. ten Hove, T. Lee, Q. Liu, I. I. Smalyukh, *Nat. Energy* **2023**, *8*, 381.
[12] C.-Q. Ma, C.-H. Xue, W. Fan, X.-J. Guo, J. Cheng, M.-C. Huang, H.-D. Wang, Y.-G. Wu, B.-Y. Liu, S.-Q. Lv, *ACS Sustainable Chem. Eng.* **2024**, *12*, 5695.
[13] S. Sen, A. Singh, C. Bera, S. Roy, K. Kailasam, *Cellulose* **2022**, *29*, 4805.
[14] Z. Wen, Z. Tang, Y. Liu, L. Zhuang, H. Yu, Y. Chu, *Adv. Mater.* **2024**, *36*, 2311870.
[15] X. Zhang, X. Cheng, Y. Si, J. Yu, B. Ding, *Chem. Eng. J.* **2022**, *433*, 133628.
[16] R. Baetens, B. P. Jelle, J. V. Thue, M. J. Tenpierik, S. Grynning, S. Uvslokk, A. Gustavsen, *Energy Build.* **2010**, *42*, 147.
[17] Y. Li, X. Liu, X. Nie, W. Yang, Y. Wang, R. Yu, J. Shui, *Adv. Funct. Mater.* **2019**, *29*, 1807624.

[18] B. Wicklein, A. Kocjan, G. Salazar-Alvarez, F. Carosio, G. Camino, M. Antonietti, L. Bergstrom, *Nat. Nanotechnol.* **2015**, *10*, 277.
[19] B. Zhao, Q. Xuan, W. Zhang, M. Hu, C. Wang, G. Pei, *Sustainable Cities and Society* **2023**, *99*, 104912.
[20] N. Herguedas, E. Carretero, *Sol. Energy Mater. Sol. Cells* **2023**, *263*, 112592.
[21] B. P. Jelle, S. E. Kalnaes, T. Gao, *Energy Build.* **2015**, *96*, 329.
[22] D. Lv, N. Fang, W. Zhang, *Infrared Phys. Technol.* **2020**, *108*, 103351.
[23] J.-W. Jang, J.-S. Kim, H. Jee, S.-H. Hong, H.-W. Seo, *Curr. Appl. Phys.* **2020**, *20*, 817.
[24] X. Yan, L. Wang, *Applied Sciences-Basel* **2020**, *10*, 6423.
[25] S. Hanauer, C. Celle, C. Crivello, H. Szambolics, D. Munoz-Rojas, D. Bellet, J.-P. Simonato, *ACS Appl. Mater. Interfaces* **2021**, *13*, 21971.
[26] A. Joudi, H. Svedung, M. Cehlin, M. Ronnelid, *Appl. Energy* **2013**, *103*, 562.
[27] Y. Wang, H. Zhou, Y. Gao, Z. Zhang, S. Liu, S. Zhong, M. Yu, J. Liu, C. Wang, *Infrared Phys. Technol.* **2022**, *121*, 104025.
[28] Y. Chen, J. Mandal, W. Li, A. Smith-Washington, C.-C. Tsai, W. Huang, S. Shrestha, N. Yu, R. P. S. Han, A. Cao, Y. Yang, *Sci. Adv.* **2020**, *6*, aaz5413.
[29] L. Yuan, X. Weng, W. Du, J. Xie, L. Deng, *J. Alloys Compd.* **2014**, *583*, 492.
[30] W.-m. Tan, L.-f. Wang, F. Yu, N. Huang, L. Wang, W.-l. Ni, J. Zhang, *Prog. Org. Coat.* **2014**, *77*, 1163.
[31] S. Fantucci, V. Serra, *Applied Sciences-Basel* **2020**, *10*, 842.
[32] Y. Peng, J.-C. Lai, X. Xiao, W. Jin, J. Zhou, Y. Yang, X. Gao, J. Tang, L. Fan, S. Fan, Z. Bao, Y. Cui, *Proceedings of the National Academy of Sciences of the USA* **2023**, *120*, 2300856120.
[33] A. Beaugendre, S. Degoutin, S. Bellayer, C. Pierlot, S. Duquesne, M. Casetta, M. Jimenez, *Prog. Org. Coat.* **2017**, *110*, 210.
[34] A. Beaugendre, C. Lemesle, S. Bellayer, S. Degoutin, S. Duquesne, M. Casetta, C. Pierlot, F. Jaime, T. Kim, M. Jimenez, *Prog. Org. Coat.* **2019**, *136*, 105269.
[35] L. Yuan, X. L. Weng, J. L. Xie, L. J. Deng, *Mater. Res. Innovations* **2015**, *19*, S1.